nature catalysis

Article

https://doi.org/10.1038/s41929-025-01463-x

Stable acidic oxygen-evolving catalyst discovery through mixed accelerations

Received: 13 January 2025

Accepted: 20 November 2025

Published online: 06 January 2026

Check for updates

Yang Bai[1,2,3,7], Kangming Li[3,4,6,7], Ning Han[1,2,7], Jiheon Kim[1,2,5], Runze Zhang[4], Suhas Mahesh[4], Ali Shayesteh Zeraati[3], Brandon R. Sutherland[3], Kelvin Chow[3], Yongxiang Liang[1], Sjoerd Hoogland[1,2], Jianan Erick Huang[1], David Sinton[2,3,5], Edward H. Sargent[1,2] ✉ & Jason Hattrick-Simpers[2,3,4] ✉

Ruthenium oxides (RuO_x) are promising alternatives to iridium catalysts for the oxygen-evolution reaction in proton-exchange membrane water electrolysis but lack stability in acid. Alloying with other elements can improve stability and performance but enlarges the search space. Material acceleration platforms combining high-throughput experiments with machine learning can accelerate catalyst discovery, yet predicting and co-optimizing synthesizability, activity and stability remain challenging. A predictive featurization workflow that links a hypothesized catalyst to its actual single- or mixed-phase synthesis and acidic oxygen-evolution reaction properties has not been reported. Here we report a hierarchical workflow, termed mixed acceleration, integrating theoretical and experimental descriptors to predict synthesis, activity and stability. Guided by mixed acceleration through 379 experiments, we identified seven ruthenium-based oxides surpassing the Pareto frontier of activity and stability. The most balanced composition, $Ru_{0.5}Zr_{0.1}Zn_{0.4}O_x$, achieved an overpotential of 194 mV at 10 mA cm^{-2} with a ruthenium dissolution rate 12 times lower than that of RuO_2.

Hydrogen is a widely used energy carrier for chemical and industrial feedstocks and for heat and power generation, with global annual demand exceeding 97 Mt (ref. 1). Currently, 99% of global hydrogen production is through fossil-fuel-intensive steam methane reforming[1]. The scalable and cost-effective production of low-carbon hydrogen will contribute to decarbonizing hard-to-abate heavy industries. Proton-exchange membrane water electrolysis (PEMWE) is a promising technology to produce green hydrogen from intermittent renewable electricity and water[2]. PEMWE cells operate in an acidic environment, which limits the selection of oxygen-evolving catalysts to those that can withstand these conditions. To date, commercial PEMWE systems rely on highly stable iridium-based catalysts. Iridium, being one of the scarcest elements (with an associated high cost, exceeding US$150 g^{-1})[3], may impose limits on large-scale deployment[4].

RuO_2 is a promising alternative, with lower cost and high activity for the oxygen-evolution reaction (OER, the limiting half-reaction in water electrolysis); however, to date, its stability has been poor in acidic conditions. A commonly used approach to stabilize ruthenium-based catalysts is through the formation of multimetal oxides[5,6]. The design space of ruthenium-based multimetal oxides is vast and grows combinatorially with the number of elements. For example, there are over 2 billion unique combinations of inorganic quaternary compounds

[1]Department of Electrical and Computer Engineering, University of Toronto, Toronto, Ontario, Canada. [2]The Alliance for AI-Accelerated Materials Discovery (A3MD), University of Toronto, Toronto, Ontario, Canada. [3]Acceleration Consortium, University of Toronto, Toronto, Ontario, Canada. [4]Department of Materials Science and Engineering, University of Toronto, Toronto, Ontario, Canada. [5]Department of Mechanical and Industrial Engineering, University of Toronto, Toronto, Ontario, Canada. [6]Present address: Physical Science and Engineering Division, King Abdullah University of Science and Technology, Thuwal, Saudi Arabia. [7]These authors contributed equally: Yang Bai, Kangming Li, Ning Han. ✉e-mail: ted.sargent@utoronto.ca; jason.hattrick.simpers@utoronto.ca

with feasible stoichiometries[7]. Both machine learning (ML) and high-throughput (HT) experimentation can be used to accelerate the exploration of inorganic chemical space[8]. However, predicting stable OER catalysts remains challenging due to the lack of suitable descriptors for assessing material stability in OER conditions[9–12]. Even when promising OER stable catalysts are predicted computationally, experimental validation is challenging, costly and time consuming—with no guarantee that candidates can even be synthesized in their predicted forms because many synthesis pathways result in mixed-phase, rather than single-phase, materials[13–15]. There are no reports of a joint experimental–computational featurization workflow that can link synthesizability, activity and stability of single- or mixed-phase catalysts for acidic OERs.

To explore mixed-metal oxide space more effectively, address challenges in materials descriptions, and bridge the gap between predicted candidates and experimental synthesis[16,17], we developed a hierarchical multimodel workflow termed mixed acceleration (MA). MA integrates hierarchical modelling, transfer learning and intermediate experimental characterization to enable accurate prediction of complex properties and to incorporate multiphase materials into ML-guided discovery. This workflow includes three ML models: one for determining the success of materials synthesis, one for assessing the OER activity of materials, and a final model that combines experiment-derived descriptors—such as structure, composition and OER activity—with presynthesis descriptors to predict catalyst OER stability in acidic conditions (see Supplementary Discussion for details). To obtain experimental descriptors efficiently for accurate OER stability predictions, we use HT experiments that reduce the time to acquire the structure, composition and OER activity to about 10 min per material. This is significantly faster than traditional OER stability tests, which take hundreds of hours for a single material. While predictions cannot fully replace experimental stability testing, they help avoid time-consuming tests on unpromising materials, saving time. Another advantage of MA is its applicability to both single-phase and multiphase materials, addressing a bottleneck in artificial intelligence (AI)-driven catalysis research[18]. Using MA, we identified seven ruthenium-based oxides that extend beyond the established Pareto frontier of OER activity and stability. Among them, $Ru_{0.5}Zr_{0.1}Zn_{0.4}O_x$ achieved an overpotential of 194 mV at 10 mA cm^{-2} and exhibited a ruthenium dissolution rate under acidic OER conditions 12 times lower than that of RuO_2.

Results

Overview of the MA workflow

The MA workflow levers ML, combined with HT experiments, to generate additional postsynthesis descriptors, the goal being to predict OER stability in acidic media. This workflow includes modular HT platforms (see Supplementary Methods for details) for synthesis, characterization and electrocatalytic performance testing[19], along with three ML models. The ML models are designed to predict: the synthesis outcome of a sol–gel reaction; whether the material exhibits high OER activity (that is, with an overpotential at 10 mA/cm^2 below 220 mV); and the OER stability of the material, measured as the ruthenium dissolution of catalyst under chronopotentiometry measurements at a current density of 10 mA cm^{-2} over 2 h.

The MA process explores ternary and quaternary metal oxides as electrocatalysts for stable acidic OERs. First, the sol–gel model eliminates combinations unlikely to form gels. From the gel-forming candidates, the OER activity model selects those with potential high activity. These materials undergo HT synthesis and characterization (X-ray diffraction (XRD), X-ray fluorescence (XRF) and OER activity testing). Experimental results, combined with presynthesis descriptors, such as elemental features, are then used to predict OER stability. The most promising candidates are then validated experimentally (Fig. 1a,b).

Five rounds of experiments (Fig. 1c) were executed to test the effectiveness of the MA approach in identifying ruthenium-based catalysts with high stability from a chemical space spanning ruthenium and 42 other elements, with a particular emphasis on covering elements with low toxicity and radioactivity. In total, 379 experiments were conducted in five sequential rounds of 100, 50, 50, 50, 100 experiments with an additional 29 experiments conducted for reproducibility evaluation. To create an initial dataset, the first iteration (I1) focused on ternary systems of Ru–O and one other element, aiming to maximize elemental coverage through ternary combinations. The second iteration (I2) explored quaternary compositions that were randomly selected from the target chemical space (47,000 possible composition combinations; see Supplementary Discussion for details). It served as the baseline to compare to subsequent ML-guided iterations. The third iteration (I3) was guided by expert intuition based on the experimental results obtained in the first two rounds to select materials. The fourth iteration (I4) was based on a gelation model and an OER activity model to select catalysts that are predicted to be both synthesizable (via the sol–gel process) and highly active. Finally, the fifth iteration (I5) was fully guided by the MA framework to identify stable catalysts within this subset. The results from previous iterations were assumed known and used as training data for I4 and I5. Although we present the MA-guided experiment as I5, the intended workflow is to initialize with an existing dataset and directly apply the MA framework for candidate selection. Iterations 1–4 were included to benchmark the MA strategy against other discovery approaches, and are not required steps for implementing the proposed MA workflow.

Materials synthesis via sol–gel reaction

Sol–gel is the chosen catalyst synthesis method in this study to accommodate a wide range of elements and compounds, simultaneously allowing precise control over chemical composition and producing highly homogeneous materials[20,21]. However, not all sol–gel reactions successfully form gels, as outcomes depend heavily on the reactants used. To identify precursor combinations that could lead to successful gelation, we applied ML methods, utilizing gradient-boosting trees implemented in the XGBoost library. To extract chemical information from precursors, we explored different descriptor sets based on elemental properties using the Matminer package[22]. We implemented a transfer learning approach, in which we explored different sets of elemental embeddings extracted from deep learning models pretrained on literature texts or computational data[23]. Among them, the elemental representation of the MEGNet model[24], a crystal graph neural network trained on the Materials Project formation energy data, was found to be the most effective in improving synthesis prediction accuracy (see Supplementary Discussion for details). The inclusion of these embeddings increased the model's F1 score from 0.79 to 0.89 (Supplementary Fig. 3).

From a total of 379 candidates tested, 294 were successfully synthesized using sol–gel methods. Figure 2b illustrates that without the gelation model, ternary oxides (I1) achieved an 80% success rate in gelation, while quaternary oxides achieved about 60% (I2 and I3). The higher success rate for ternary oxides is attributed to fewer elements, allowing more controlled synthesis conditions. We then incorporated the gelation model to guide the I4 to only select gelable candidates, which achieved a 100% gelation success rate over 50 synthesized materials, validating the model's efficacy. Overall, our predictive gelation model achieved 91% precision across these 379 experimental results (Supplementary Fig. 2).

Shapley additive explanations (SHAP) values[25] were used to quantify the impact of material features and experimental conditions for the gelation reaction in Fig. 2c. Due to the opaque nature of embeddings, our SHAP analysis used a ML model without element embeddings to improve interpretability. In this study, we focused primarily on the properties related to solvents and precursors in the sol–gel reaction for SHAP.

Ethanol was the primary reaction solvent, with water occasionally added to dissolve salts containing alkali metals that are insoluble

https://doi.org/10.1038/s41929-025-01463-x

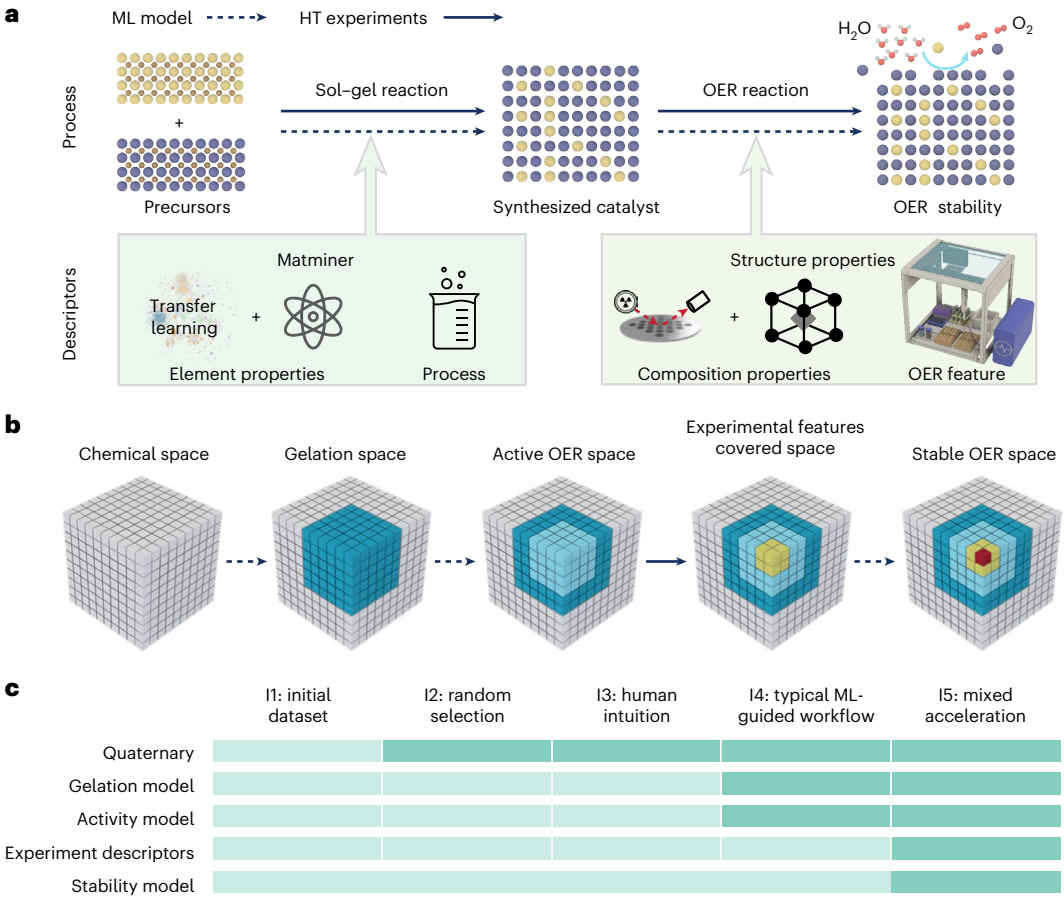

Fig. 1 | MA workflow. a, The MA spans the full process of catalyst precursor selection through synthesis to performance evaluation (OER stability and activity). Synthesis descriptors are established through gelation prediction (which incorporates reaction process parameters and elemental information from precursors using Matminer and transfer learning). OER reaction descriptors are developed using a stability model that utilizes compositional information (coordinating HT experimental results with structure-derived properties from the Materials Project) and electrochemical features (experimental OER activity results). **b**, Illustration of the gradual narrowing of discovered stable OER catalyst space using MA. The solid arrows indicate parts accelerated by HT experiments, and the dashed arrows indicate parts accelerated by ML models. **c**, Five iterative experiments (I1–I5) were conducted with different guidelines, where lighter shading indicates areas not covered in a specific iteration and darker shading highlights included components.

in ethanol. However, the presence of water was found to negatively impact gelation success, as shown by negative SHAP values (Fig. 2c). This is probably due to the hydrolysis of metal chlorides in water, leading to the formation of insoluble precipitates that impede precursor reactions. Additionally, water alters the solvent's polarity and properties, affecting reaction kinetics and potentially disrupting the gelation process[26]. In contrast, low water fractions or anhydrous conditions using propylene oxide and ethanol effectively dissolved and dispersed precursors, facilitating gel formation.

Electronic structure features of precursors, such as ionic character, electronegativity and anion electron affinity (EA), were ranked as the second, third and fourth most impactful features in SHAP analysis, following the reaction solvent. Ionic character showed a positive correlation with gelation rates, probably because higher ionic character enhances interactions with solvents and gel agents such as propylene oxide, promoting sol–gel formation and stabilizing the gel network[26,27]. Conversely, anion EA was negatively correlated with gelation rates. In this study, only nitrate and chloride salts were used, and the higher EA value of nitrate compared to chloride suggests that chloride salts are more effective in facilitating sol–gel reactions than are nitrates[28,29].

OER performance in acidic medium

The two primary co-optimization targets for OER electrocatalysts are activity and stability. Here we used overpotentials at 10 mA cm^{-2} as the metric for catalyst activity. For OER stability, some studies use potential changes under a certain current density as a proxy[30,31]. Potential is a complex parameter influenced by multiple factors, such as bubble effects[32]. As shown in Supplementary Fig. 7, the lack of correlation between potential changes and ruthenium dissolution further suggests that potential fluctuations do not reliably reflect material degradation. To better evaluate OER stability, Geiger et al. proposed the S-number[33], which uses the amount of dissolved iridium in relation to the evolved oxygen as an independent metric to estimate lifetimes. In this study, we conducted 2-h constant-current OER tests at 10 mA cm^{-2}. Similar to the S-number approach, we used the percentage of ruthenium leaching during these tests to estimate material lifetimes, under the assumption that all electrons participate in the OER reaction. Dissolution data were collected through inductively coupled plasma optical emission spectroscopy (ICP-OES) measurements of the electrolytes after the OER.

An XGBoost classification model was trained to predict the OER activity using the same Matminer descriptor set as in the gelation model, with an F1 accuracy of 81%. The element embeddings were not used here because they did not contribute to accuracy improvement. As shown in Fig. 3a, the proportion of materials exhibiting overpotentials higher than 220 mV at 10 mA cm^{-2} is reduced to 12% in the I4 guided by the activity model, compared to 32%, 100% and 54% in the I1, I2 and I3, respectively. The median overpotentials for the first four iterations were 206, 400, 225 and 171 mV, respectively, highlighting the increased likelihood of selecting catalysts with higher activity under the guidance of the OER activity model. Following activity testing, materials with

https://doi.org/10.1038/s41929-025-01463-x

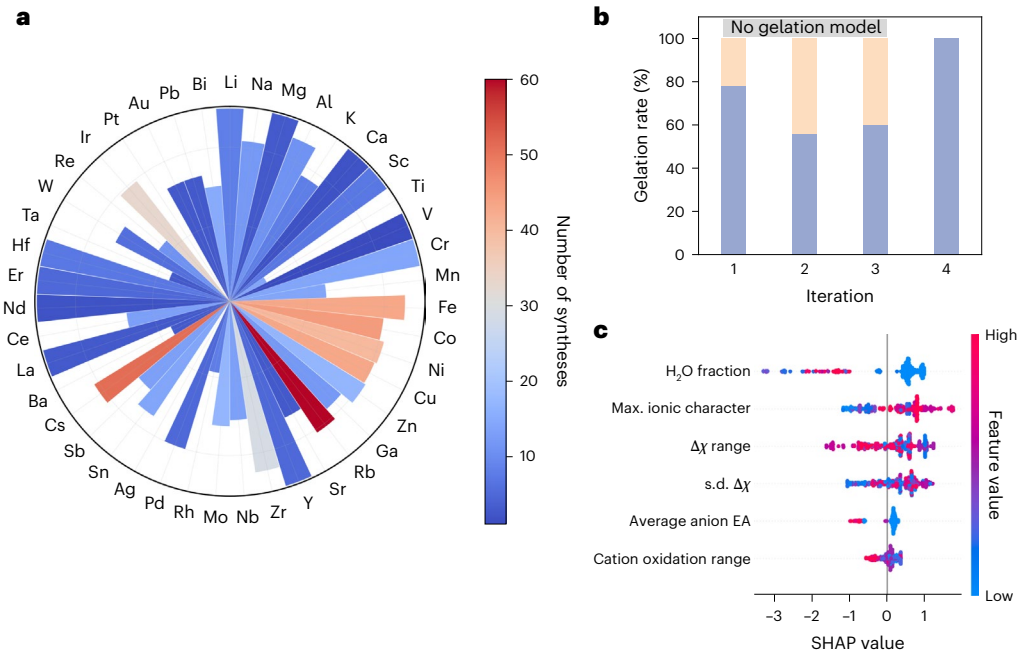

Fig. 2 | Mixed-metal ruthenium oxide sol–gel synthesis. a, Gelation results for elements involved in the study (excluding ruthenium). The bar length represents the gelation success rate for each element (the outermost circle indicates a 100% success rate); the colour indicates the frequency of the element's occurrence in the 379 synthesis attempts. Six synthesis attempts with precursors containing silver and five attempts with precursors containing platinum were made, but none were successful. **b**, Comparison of synthesis outcomes with and without the gelation model's guidance: purple bars indicate successful gelation; pink bars represent gelation failure. **c**, SHAP analysis of the gelation model, with features ranked by their overall SHAP feature importance from top to bottom.

overpotentials smaller than 250 mV at 10 mA cm^{-2} were selected for further stability testing, as detailed in the Methods.

After verifying the activity model's effectiveness in the I4, we employed the MA strategy in the I5 to search for stable OER catalysts. Figure 3b illustrates that the overall OER stability in the I5 was significantly improved compared to results without MA guidance. The median ruthenium dissolution rates for the I1, I3, I4 and I5 were 0.72%, 1.74%, 0.79% and 0.34%, respectively. Data from the I2 were excluded because most syntheses either failed or did not lead to materials with good OER activity (overpotential >300 mV), resulting in only one valid data point (Supplementary Table 1). More than 90% of materials from the I5, guided by the MA strategy, showed ruthenium dissolution rates below 1% (Fig. 3c). These results provide experimental evidence that the MA approach is effective.

It is sometimes held that there may exist a trade-off between catalytic overpotential and stability: that is, that highly active catalysts tend to have lower stability in acidic OER conditions[34,35]. Such a trade-off would manifest as a Pareto frontier in the multiobjective optimization of active and stable catalysts, as shown in Fig. 3c. Notably, the MA-guided experiments in the fifth round were able to push the boundaries of the Pareto frontier (dashed line) formed by the first four rounds of experiments. Seven materials exceeded the Pareto frontier, namely, $Ru_{0.5}Zr_{0.1}Zn_{0.4}O_x$, $Ru_{0.5}Zn_{0.4}Ni_{0.1}O_x$, $Ru_{0.6}Zn_{0.3}Cu_{0.1}O_x$, $Ru_{0.6}Zr_{0.1}Zn_{0.3}O_x$, $Ru_{0.5}Mg_{0.1}Zn_{0.4}O_x$, $Ru_{0.8}Fe_{0.1}Ni_{0.1}O_x$ and $Ru_{0.7}Cs_{0.2}Rb_{0.1}O_x$, ranked here by their ruthenium dissolution rates from low to high (Supplementary Fig. 8). Notably, zinc appeared in five of the materials with the lowest ruthenium dissolution rates, while zirconium and nickel featured twice. Of particular interest, $Ru_{0.5}Zr_{0.1}Zn_{0.4}O_x$ demonstrated a ruthenium dissolution rate 12 times lower than that of RuO_2 under acidic OER conditions.

Figure 3d,e summarizes the distribution of OER activity and stability across different dopants. Elements such as iron, cobalt, copper and nickel improve OER activity, consistent with previous findings attributing enhancements to favourable electronic interactions with ruthenium[31–33,36,37]. Alkali metals (lithium, sodium, rubidium) frequently appear in high-activity compositions, and quaternary systems incorporating alkali metals generally outperform their ternary counterparts (Supplementary Fig. 16)[38]. However, these alkali-metal-containing catalysts exhibit poorer stability (Fig. 3e), probably due to their tendency to facilitate overoxidation of ruthenium during catalyst restructuring.

In contrast, dopants such as zirconium, zinc and hafnium correlate with reduced ruthenium dissolution, suggesting their potential in stabilizing ruthenium-based catalysts[39]. To examine dopant roles further, we conducted ICP-OES analyses on additional transition and alkali metals from initial stability screening (Supplementary Fig. 21). Most non-ruthenium elements showed over 10% dissolution after 2 h, indicating that they are unlikely primary active sites. Instead, they appear to modulate ruthenium's local environment, influencing its restructuring and subsequent stability.

We then studied in greater depth seven catalysts beyond the Pareto front, along with the most active catalyst from the initial screening ($Ru_{0.5}Rb_{0.2}Ni_{0.3}O_x$), and performed extended 20-h chronopotentiometric tests at 10 mA cm^{-2}. Electrolytes collected at 0, 2, 5 and 20 h (with the 0-h sample taken after initial cyclic voltammetry cycling, 1.0–1.2 V versus RHE (reversible hydrogen electrode)) were analysed by ICP-OES (Supplementary Figs. 22–29). All eight catalysts showed stable potentials throughout the tests. The majority of metal dissolution occurred within the first 2 h, indicating early-stage catalyst reconstruction. Zinc, rubidium, copper and magnesium exhibited initial dissolution of >20%, while the dissolution of nickel and iron was ~10%. In contrast, ruthenium and zirconium were stable with <1% dissolution. Notably, zirconium-containing catalysts showed significantly less and slower zinc dissolution (~20%) compared with their zirconium-free counterparts (~50%), highlighting zirconium's role in stabilizing the catalyst structure.

X-ray photoelectron spectroscopy analysis (Supplementary Figs. 31–38 and Supplementary Table 2) showed that the seven Pareto-front-surpassing catalysts initially exhibited lower ruthenium oxidation states than the highly active $Ru_{0.5}Rb_{0.2}Ni_{0.3}O_x$, consistent with their enhanced stability under acidic OER. After 20 h of operation,

https://doi.org/10.1038/s41929-025-01463-x

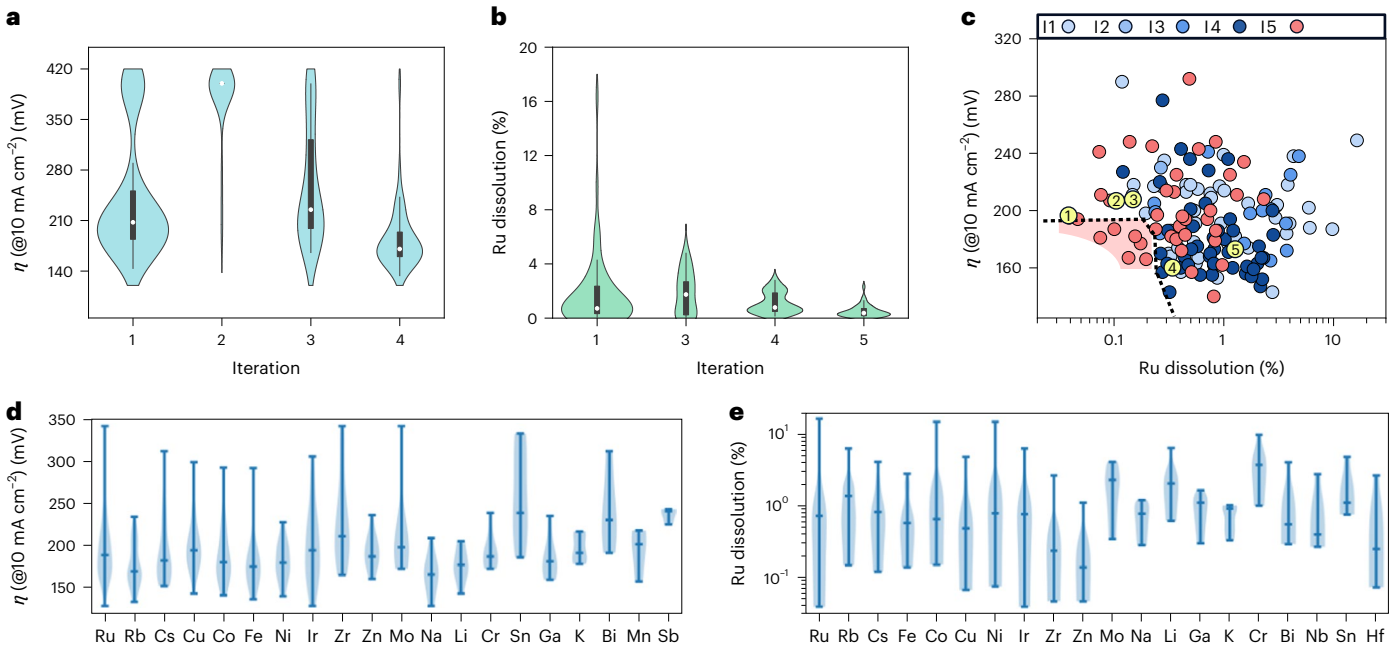

Fig. 3 | OER performance evaluation. a, Distribution of overpotential (η) data across experimental iterations: without the OER activity model (I1, I2 and I3) and with the OER activity model (I4). **b**, Distribution of ruthenium dissolution data across experimental iterations: without the OER stability model (I1, I3 and I4) and with the MA (I5). In **a**,**b** the solid black boxes represent the interquartile range (IQR, 25–75%), the black whiskers denote the range within 1.5 × IQR and the white dots indicate the median. **c**, Plot of overpotential versus ruthenium dissolution for catalysts (blue, I1–I4; red, I5; yellow, reported ruthenium-based catalysts). The dashed line represents the Pareto frontier formed by the first four rounds of experimental results and includes results of the most efficient previously reported ruthenium-based OER catalysts in acidic media: 1, $IrRuO_x$ (ref. 40); 2, $ZnRuO_x$ (ref. 39); 3, $CoRuO_x$ (ref. 46); 4, $MnRuO_x$ (ref. 47); 5, $CrRuO_x$ (ref. 48). The reported compositions were synthesized using the sol–gel method and measured under the same high-throughput OER measurement conditions. **d**,**e**, Overpotential at 10 mA cm^{-2} (**d**) and ruthenium dissolution of the oxides (**e**) varies by element type. Elements in **d**,**e** are arranged from left to right based on the frequency of occurrence in catalysts with valid data. In these violin plots, the horizontal lines within each violin represent the minimum, median and maximum values, and the width of the shaded area indicates the distribution density of data points. All OER measurements in this study were performed in 0.5 M H_2SO_4 electrolyte. In **b**,**c**,**e** ruthenium dissolution values represent the amount of ruthenium detected in the electrolyte after 2 h of chronopotentiometry at 10 mA cm^{-2}, determined by quantifying the dissolved ruthenium concentration in the collected electrolyte.

six of the more-stable catalysts showed minimal or increased Ru^{4+} content, indicating reconstruction toward a more active Ru^{4+} state while retaining sufficient Ru^{3+} to preserve structural stability[40,41]. Zirconium-containing samples showed <3% shift in ruthenium oxidation state, while zirconium-free samples exceeded 10%, suggesting zirconium moderates restructuring. In contrast, $Ru_{0.5}Rb_{0.2}Ni_{0.3}O_x$ showed a significant decrease in Ru^{4+}, probably reflecting further oxidation of ruthenium to higher-valence states during OER, consistent with its elevated ruthenium dissolution. A similar trend in $Ru_{0.7}Cs_{0.2}Rb_{0.1}O_x$ further suggests that alkali metals may promote ruthenium destabilization.

Electrochemical impedance spectroscopy (Supplementary Figs. 39–46) at 0, 2, 5 and 20 h (1.5 V versus RHE) was conducted to assess changes in active surface area and intrinsic activity. The double-layer capacitance (C_{dl}) and charge-transfer resistance (R_{ct}) were objectively determined using AutoEIS[42], an automated Bayesian inference tool for equivalent circuit selection. C_{dl} generally remained stable or slightly decreased post-activation, indicating that the dissolution of elements such as copper and nickel did not substantially enhance the electrochemically active surface area. R_{ct} showed mild early increases before stabilizing, further supporting that major ruthenium reconstruction occurred during the initial stage of the OER reaction.

These findings appear to indicate that doping ruthenium with acid-labile elements (such as zinc, nickel and copper) modulates its electronic structure and local coordination environment in a manner that suppresses ruthenium overoxidation during catalyst synthesis and in the ensuing acidic OER operation. This effect is observed even though these transient dopants are largely leached out during the early stages of the OER. Incorporating zirconium further reduces the extent of excess reconstruction, contributing also to stability. In contrast, doping with alkali metals (for example, rubidium and caesium) promotes ruthenium overoxidation under OER conditions, which initially boosts catalytic activity but ultimately accelerates catalyst degradation and reduces durability. Taken together, these observations highlight the element-specific nature of the dopant effects on catalyst performance and stability in acidic OERs, underscoring the importance of judicious dopant selection in designing robust, durable OER catalysts[43].

Mixed acceleration for discovering higher-stability catalysts for acidic OERs

Testing the OER stability of catalysts is far more challenging than evaluating activity. Stability tests require significantly longer durations and involve multidimensional analyses, such as monitoring voltage changes during chronopotentiometry tests and measuring catalyst dissolution using ICP. Improving the predictive capabilities of OER stability, thereby minimizing the number of time-consuming experimental stability tests required, is critical to accelerate the catalyst discovery process. In our MA approach, we predict OER stability using a combination of presynthesis and experimental descriptors. Presynthesis descriptors include the chemical properties of precursors and synthesis conditions. Experimental descriptors, such as OER overpotential at 10 mA cm^{-2}, and XRF and XRD analyses, provide detailed insights into the composition and structure of synthesized materials. Overpotential serves as a composite measure for unknown factors influencing OER performance (additional kinetic descriptors such as Tafel slope were also tested, but did not further improve model performance; Supplementary Fig. 11). Based on XRD spectra for our mixed-phase materials, we label crystal

https://doi.org/10.1038/s41929-025-01463-x

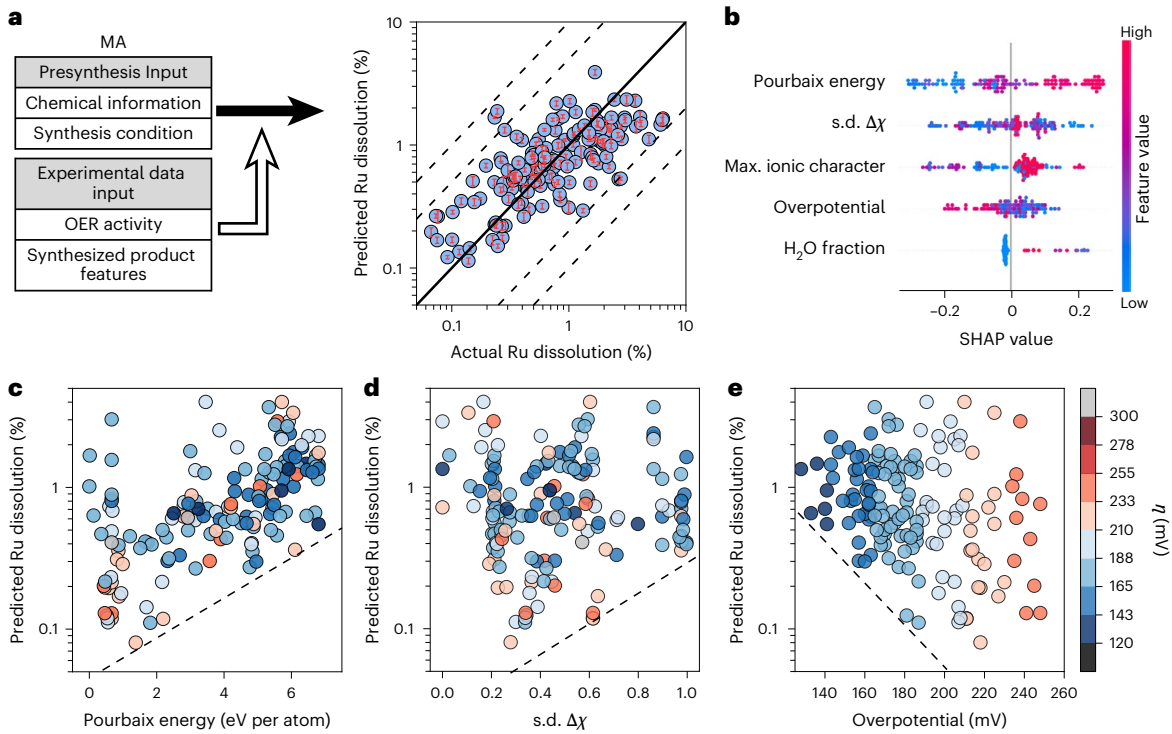

Fig. 4 | OER stability predictions with MA. a, Using MA for materials discovery, presynthesis data (chemical information and synthesis conditions) plus experimental data (OER activity and features of synthesized materials) are used to describe materials. The output shows an $R_{Pearson}$ of 0.725 for the actual versus predicted plot of ruthenium dissolution after 2 h of chronopotentiometry at 10 mA cm^{-2} in 0.5 M H_2SO_4 electrolyte. The solid line indicates perfect predicted correlation, and the dashed lines show the 5× and 10× error. The error bar for predicted ruthenium dissolution is $\pm\sigma$, where σ is the sample s.d. obtained from ten independently initialized runs of 20-fold cross-validation. σ is representative of model uncertainty and a range of $\pm 1.96\sigma$ corresponds to a two-sided 95% confidence interval for an individual prediction. **b**, SHAP analysis for the feature contribution to the stability prediction in MA. **c**–**e**, The predicted ruthenium dissolution versus the Pourbaix decomposition energy weighted by phase fractions (**c**), the s.d. of the electronegativity difference between elements in the material (**d**) and the measured overpotential at 10 mA cm^{-2} (**e**). The colour bar for **c**–**e** indicates the overpotential at 10 mA cm^{-2}.

structures and retrieve corresponding Materials Project data, which includes various density functional theory (DFT)-computed properties such as bandgap, valence band maximum and Pourbaix decomposition energies at different conditions. We then weigh the properties of different structures according to the area of their main peaks in the XRD spectrum (as a proxy for phase fractions) to describe the mixed phase (see Supplementary Methods and Supplementary Fig. 12 for details). As such, these experimentally derived descriptors incorporate information from both experimental measurements and DFT calculations. It is worth highlighting that our MA strategy does not require the most accurate quantum-mechanical simulations to generate descriptors that quantitatively match experiment. Our MA framework shows that even modestly accurate DFT results, as long as they capture the experimental trends, can be sufficient to build effective ML models. This is because the models leverage both experimental and computational data and calibrate the DFT inputs to experimental reality, hence enabling the direct integration of DFT datasets that are widely available in public repositories.

The Pearson correlation coefficient ($R_{Pearson}$) was used to evaluate the OER stability model performance, and the mean absolute percentage error served as a reference for the accuracy of the predicted values compared with actual values. With the MA strategy, the model achieved an $R_{Pearson}$ value of 0.725 and a mean absolute percentage error of 65.3%. Additionally, the maximum relative prediction uncertainty for each material was below 14%, much lower than 64% for the model only with presynthesis information (Supplementary Fig. 10). Notably, the MA strategy eliminated all predictions with more than 10-fold errors and reduced 60% of predictions with 5- to 10-fold errors compared with the presynthesis-only model, demonstrating a significant improvement in accuracy by incorporating experimental descriptors.

SHAP analysis was used to evaluate feature contribution to OER stability for the model that was used in MA (Fig. 4b). Pourbaix energy, derived from experimentally obtained descriptors, ranked as the most important feature and showed a positive correlation with ruthenium dissolution. This feature, which cannot be accurately captured without experimental input for composition, underscores the critical role of experimental descriptors in OER stability predictions. Pourbaix decomposition energy measures the thermodynamic stability of a material in aqueous environments and represents the energy change associated with the decomposition of a compound into stable species under specific electrochemical conditions[44]. A correlation analysis across all studied materials (Supplementary Fig. 49) revealed that zirconium content is most negatively correlated with Pourbaix decomposition energy: that is, zirconium enhances thermodynamic stability under electrochemical conditions and thereby improves overall materials stability. This finding is consistent with the trends discussed earlier. As shown in Fig. 4c, the lower limit of ruthenium dissolution increases with rising Pourbaix decomposition energy, consistent with the fact that lower Pourbaix decomposition energy is beneficial for minimizing ruthenium dissolution during the OER. Electronegativity (Fig. 4d) and ionic character emerged as the second and third most important chemical features, and also showed a positive correlation with ruthenium dissolution, consistent with previous findings[18]. In contrast to these top three features, which were positively correlated with ruthenium dissolution, the experimental descriptor overpotential exhibited an inverse relationship. As illustrated in Fig. 4e, the lower limit of ruthenium dissolution decreases as overpotential decreases, aligning with our experimental observations in Fig. 3c.

Therefore, by conducting rapid OER activity tests and combining the results with Pourbaix energy, electronegativity and ionic character information, we can accurately predict OER stability before conducting time-consuming stability tests. This approach avoids spending hundreds or thousands of hours on low-success materials, thereby accelerating material discovery.

Conclusion

We developed an MA workflow that integrates hierarchical models with experimental descriptors to predict the OER activity and the stability of catalysts under acidic conditions. MA-guided experiments pushed the Pareto frontier of OER activity and stability beyond other strategies explored in this research, identifying seven standout ruthenium-based catalysts. $Ru_{0.5}Zr_{0.1}Zn_{0.4}O_x$, an iridium-free catalyst, demonstrated a ruthenium dissolution rate of 0.046%, comparable to 0.039% for $Ru0._5Ir_{0.5}O_x$, underscoring the potential of zirconium and zinc as effective alternatives to iridium for stabilizing catalysts. Additionally, $Ru_{0.6}Ir_{0.2}Na_{0.2}O_x$ achieved an overpotential of 128 mV at 10 mA cm^{-2}, while $Ru_{0.5}Rb_{0.2}Ni_{0.3}O_x$, another iridium-free catalyst, exhibited 140 mV. Most of these dopants do not serve as primary OER active sites; instead, they influence catalyst performance by modulating ruthenium oxidation states during synthesis and steering ruthenium reconstruction during operation. Elucidating these dopant-mediated restructuring pathways will help assist in the design of stable and active catalysts for acidic OERs.

The present research addresses the complex challenge of acidic OER stability by breaking it into three manageable steps using hierarchical models: materials synthesis, OER activity, and OER stability. We use experimental descriptors that enable a three-orders-of-magnitude acceleration over traditional stability measurements that further enhance material representation accuracy and improve prediction reliability. The approach is not limited to ruthenium-based materials and could be used for finding non-noble metal catalysts for acidic OERs. In future work, these descriptors can be seamlessly integrated into autonomous, self-driving laboratories to further accelerate the workflow and enable full AI-agent guided experimentation. This MA approach bridges the gap between theoretical material representations and practical OER stability, enabling more precise and efficient predictions of oxygen-evolving catalysts.

Methods

Sol–gel reaction synthesis

All precursors were dissolved in ethanol at a concentration of 0.675 mol l^{-1}. For precursors insoluble in ethanol, water was used to maintain the same concentration. Using a Chemspeed Swing system, different precursors were accurately dispensed into 15-ml round-bottom centrifuge tubes, with a total volume of 1 ml per tube. The solution was shaken for 10 min to ensure thorough mixing of the precursors. Then, 0.5 ml of propylene oxide was added to the mixture, followed by an additional 5 min of shaking and 1 day of standing to promote gel formation.

For the gelled samples, 5 ml of acetone was added to each centrifuge tube, the mixture was centrifuged and the supernatant was discarded. This acetone washing process was repeated three times. Subsequently, 5 ml of water was added, followed by centrifugation and removal of the supernatant. The supernatant-removal steps were manually performed, while all other steps were automated using the Chemspeed system. After centrifugation, the powder was obtained by drying the gel in a vacuum oven for 1 day and annealing it at 400 °C for 2 h to produce crystalline samples. Finally, a high-throughput ball miller (MSK-SFM-50, MTI) was used to produce fine powders. This semiautomated synthesis process handled 50 samples per batch. To evaluate scalability, we scaled up the synthesis of $Ru_{0.5}Zr_{0.1}Zn_{0.4}O_x$ by 5× and observed comparable yield; the overpotential at 10 mA cm^{-2} differed by only 5.9 mV, which can be considered within the range of experimental error, demonstrating the robustness of the synthesis approach for larger-scale production (Supplementary Fig. 47).

Materials characterization

XRD measurements were conducted using a Bruker D8 diffractometer with a copper Kα source. XRF analysis was performed with a Fischerscope XRF-XDAL 237 SDD. A custom mould allowed us to consistently drop-cast 60 different samples on a 3-inch silicon wafer (Supplementary Fig. 5). Combined with the characterization equipment's controllable moving sample stage, this set-up enabled automatic testing of 60 samples per batch for both XRF and XRD (see Supplementary Methods for details). Transmission electron microscopy (TEM) and high-resolution TEM were performed using JEM-2100F and JEM-F200 (JEOL) microscopes, respectively, at an acceleration voltage of 200 kV. The TEM samples were placed on carbon films on 200-mesh gold grids. The dissolution rate of the catalysts was analysed using the iCAP PRO XP ICP-OES system. For ICP analysis, samples were prepared by extracting a 3-ml volume of electrolyte from the electrochemical cell. Calibration standards for ruthenium elemental analysis were prepared at concentrations of 0.1, 1 and 50 ppm.

Electrocatalytic measurement

All electrocatalytic experiments were conducted using an automated OER testing platform (Supplementary Fig. 6)[19], which integrates a liquid-handling robot (Opentrons OT-2), a potentiostat (Biologic VSP-3e), custom-designed array reactors and a modular electrode holder. The OT-2 was chosen for its ease of use and Python API integration, enabling programmable and reproducible ink deposition. The array reactors were CNC-milled from polyether ether ketone for enhanced chemical resistance. Catalyst ink preparation and electrode fabrication were carried out as follows: 5 mg of catalyst powder was dispersed in 250 µl of a mixed solvent (water:ethanol, 4:1 v/v) containing 5 wt% Nafion as a binder. The ink was drop-cast onto carbon paper substrates (AvCarb MGL190, Fuel Cell Store) and dried in a furnace at 70 °C for 2 h to ensure good adhesion and solvent removal. All electrochemical tests were performed in a three-electrode configuration using a Biologic VSP-3e potentiostat. The electrolyte was 0.5 M H_2SO_4 (ACS grade), prepared with ultrapure water (18.2 MΩ·cm). A platinum wire was used as the counter-electrode, and an Ag/AgCl (3 M KCl) electrode served as the reference. All potentials were converted to the RHE scale using the following equation:

$$E_{RHE} = E_{Ag/AgCl} + 0.210V + 0.059 \times pH \quad (1)$$

Linear sweep voltammetry was then conducted from 1 V to 1.65 V versus RHE at a scan rate of 5 mV s^{-1} to prepare polarization curves. The overpotential at 10 mA cm^{-2} is used to determine the OER activity of the samples. Finally, chronopotentiometry holds the current density at 10 mA cm^{-2} for 2 h to evaluate short-term stability. Electrolyte samples are subsequently collected for ICP-OES measurement. Details are shown in the Supplementary Methods.

ML methods

First, we explored several descriptor-based ML methods, including Gaussian processes, random forest and boosting trees. We found the gradient-boosting algorithm as implemented in the XGBoost[45] package to be the most accurate one and therefore used it throughout the work. The hyperparameter tuning was performed using the nested cross-validation method. For the classification and regression models, we used five parallel trees each with 200 boosting rounds, a learning rate of 0.2, a regularization strength of 0.5 for both L1 and L2 regularization (see Supplementary Fig. 48 for justification), and a subsample ratio of feature columns of 0.5 for each tree and for each depth level. For classification models, we set the sample weights to be inversely proportional to the numbers of class instances.

We used the Matminer package to generate compositional descriptors from precursor information. We used statistics (maximum, minimum, range and s.d.) of the elemental attributes (for example, oxidation states, ion properties, electron affinity, electronegativity) to describe each precursor combination. For the gelation model, we additionally considered the element embeddings from the MEGNet model trained on Materials Project formation energy data. We treated these embeddings in a way similar to elemental attributes to create additional descriptors.

To create experimentally informed descriptors for each sample, we retrieved from Materials Project the DFT-calculated Pourbaix decomposition energies for the phases identified through HT XRD characterization. For each multiphase sample, we calculated a weighted Pourbaix decomposition energy by averaging the Pourbaix decomposition energies by the corresponding XRD peak areas of the phases (see Supplementary Fig. 12 for details).

Data availability

The authors declare that all data supporting the findings of this study are available within the paper and the Supplementary Information files, or from the corresponding authors upon request. Data used in ML models are available from GitHub via https://github.com/kangming-li/Stable-OER-Catalyst-Discovery-Through-Mixed-Acceleration.

Code availability

The code used in this work is available from GitHub via https://github.com/kangming-li/Stable-OER-Catalyst-Discovery-Through-Mixed-Acceleration.

References

1. *Global Hydrogen Review 2024* www.iea.org (International Energy Agency, 2024).
2. Jiao, K. et al. Designing the next generation of proton-exchange membrane fuel cells. *Nature* **595**, 361–369 (2021).
3. Wan, R. et al. Earth-abundant electrocatalysts for acidic oxygen evolution. *Nat. Catal.* **7**, 1288–1304 (2024).
4. An, L. et al. Recent development of oxygen evolution electrocatalysts in acidic environment. *Adv. Mater.* **33**, 2006328 (2021).
5. Abed, J. et al. Pourbaix machine learning framework identifies acidic water oxidation catalysts exhibiting suppressed ruthenium dissolution. *J. Am. Chem. Soc.* **146**, 15740–15750 (2024).
6. Li, J. et al. A review on highly efficient Ru-based electrocatalysts for acidic oxygen evolution reaction. *Energy Fuels* **38**, 11521–11540 (2024).
7. Park, H., Onwuli, A., Butler, K. T. & Walsh, A. Mapping inorganic crystal chemical space. *Faraday Discuss.* **256**, 601–613 (2025).
8. Yao, Z. et al. Machine learning for a sustainable energy future. *Nat. Rev. Mater.* **8**, 202–215 (2023).
9. Sasmal, S. et al. Materials descriptors for advanced water dissociation catalysts in bipolar membranes. *Nat. Mater.* **23**, 1421–1427 (2024).
10. Liu, X., Cai, C., Zhao, W., Peng, H. J. & Wang, T. Machine learning-assisted screening of stepped alloy surfaces for C_1 catalysis. *ACS Catal.* **12**, 4252–4260 (2022).
11. Chen, Z. W., Chen, L. X., Gariepy, Z., Yao, X. & Singh, C. V. High-throughput and machine-learning accelerated design of high entropy alloy catalysts. *Trends Chem.* **4**, 577–579 (2022).
12. Vasudevan, R. K. et al. Materials science in the artificial intelligence age: high-throughput library generation, machine learning, and a pathway from correlations to the underpinning physics. *MRS Commun.* **9**, 821–838 (2019).
13. Chanussot, L. et al. Open Catalyst 2020 (OC20) dataset and community challenges. *ACS Catal.* **11**, 6059–6072 (2021).
14. Tran, R. et al. The Open Catalyst 2022 (OC22) dataset and challenges for oxide electrocatalysts. *ACS Catal.* **13**, 3066–3084 (2023).
15. Erucar, I. & Keskin, S. High-throughput molecular simulations of metal organic frameworks for CO_2 separation: opportunities and challenges. *Front Mater.* **5**, 1–6 (2018).
16. Szymanski, N. J. et al. An autonomous laboratory for the accelerated synthesis of novel materials. *Nature* **624**, 86–91 (2023).
17. Cheetham, A. K. & Seshadri, R. Artificial intelligence driving materials discovery? Perspective on the article: scaling deep learning for materials discovery. *Chem. Mater.* **36**, 3490–3495 (2024).
18. Moon, J. et al. Active learning guides discovery of a champion four-metal perovskite oxide for oxygen evolution electrocatalysis. *Nat. Mater.* **23**, 108–115 (2024).
19. Abed, J. et al. AMPERE: automated modular platform for expedited and reproducible electrochemical testing. *Digit. Discov.* **3**, 2265–2274 (2024).
20. Janani, R., Farmilo, N., Roberts, A. & Sammon, C. Sol-gel synthesis pathway and electrochemical performance of ionogels: A deeper look into the importance of alkoxysilane precursor. *J. Non Cryst. Solids* **569**, 120971 (2021).
21. Zhang, B. et al. Homogeneously dispersed multimetal oxygen-evolving catalysts. *Science* **352**, 333–337 (2016).
22. Ward, L. et al. Matminer: an open source toolkit for materials data mining. *Comput Mater. Sci.* **152**, 60–69 (2018).
23. Onwuli, A., Hegde, A. V., Nguyen, K. V. T., Butler, K. T. & Walsh, A. Element similarity in high-dimensional materials representations. *Digit. Discov.* **2**, 1558–1564 (2023).
24. Chen, C., Ye, W., Zuo, Y., Zheng, C. & Ong, S. P. Graph networks as a universal machine learning framework for molecules and crystals. *Chem. Mater.* **31**, 3564–3572 (2019).
25. Lundberg, S. M. et al. From local explanations to global understanding with explainable AI for trees. *Nat. Mach. Intell.* **2**, 56–67 (2020).
26. Kessler, V. G. & Seisenbaeva, G. A. Molecular mechanisms of the metal oxide sol-gel process and their application in approaches to thermodynamically challenging complex oxide materials. *J. Solgel Sci. Technol.* **107**, 190–200 (2023).
27. Baumann, T. F., Gash, A. E., Satcher, J. H., Leventis, N. & Steiner, S. A. in *Springer Handbook of Aerogels* (eds Aegerter, M. A., Leventis, N., Koebel, M. & Steiner, S. A., III) 419–435 https://doi.org/10.1007/978-3-030-27322-4_17 (Springer, 2023).
28. Rouwhorst, J., Ness, C., Stoyanov, S., Zaccone, A. & Schall, P. Nonequilibrium continuous phase transition in colloidal gelation with short-range attraction. *Nat. Commun.* **11**, 3558 (2020).
29. Hu, C., Lu, W., Mata, A., Nishinari, K. & Fang, Y. Ions-induced gelation of alginate: mechanisms and applications. *Int J. Biol. Macromol.* **177**, 578–588 (2021).
30. Edgington, J., Deberghes, A. & Seitz, L. C. Glassy carbon substrate oxidation effects on electrode stability for oxygen evolution reaction catalysis stability benchmarking. *ACS Appl Energy Mater.* **5**, 12206–12218 (2022).
31. Du, K. et al. Interface engineering breaks both stability and activity limits of RuO_2 for sustainable water oxidation. *Nat. Commun.* **13**, 1–9 (2022).
32. Ikeda, H. et al. Microscopic high-speed video observation of oxygen bubble generation behavior and effects of anode electrode shape on OER performance in alkaline water electrolysis. *Int J. Hydrog. Energy* **47**, 11116–11127 (2022).
33. Geiger, S. et al. The stability number as a metric for electrocatalyst stability benchmarking. *Nat. Catal.* **1**, 508–515 (2018).
34. Oener, S. Z., Bergmann, A. & Cuenya, B. R. Designing active oxides for a durable oxygen evolution reaction. *Nat. Synth.* **2**, 817–827 (2023).

35. Gao, G. et al. Recent advances in Ru/Ir-based electrocatalysts for acidic oxygen evolution reaction. *Appl Catal. B* **343**, 123584 (2024).
36. Anantharaj, S., Kundu, S. & Noda, S. The Fe effect: a review unveiling the critical roles of Fe in enhancing OER activity of Ni and Co based catalysts. *Nano Energy* **80**, 105514 (2021).
37. Wang, N. et al. Doping shortens the metal/metal distance and promotes OH coverage in non-noble acidic oxygen evolution reaction catalysts. *J. Am. Chem. Soc.* **145**, 7829–7836 (2023).
38. Qin, Y. et al. RuO_2 electronic structure and lattice strain dual engineering for enhanced acidic oxygen evolution reaction performance. *Nat. Commun.* **13**, 3784 (2022).
39. Zhang, D. et al. Construction of Zn-doped RuO_2 nanowires for efficient and stable water oxidation in acidic media. *Nat. Commun.* **14**, 2517 (2023).
40. Zhu, W. et al. Stable and oxidative charged Ru enhance the acidic oxygen evolution reaction activity in two-dimensional ruthenium–iridium oxide. *Nat. Commun.* **14**, 5365 (2023).
41. Liu, H. et al. Eliminating over-oxidation of ruthenium oxides by niobium for highly stable electrocatalytic oxygen evolution in acidic media. *Joule* **7**, 558–573 (2023).
42. Sadeghi, M. A., Zhang, R. & Hattrick-Simpers, J. AutoEIS: automated equivalent circuit modeling from electrochemical impedance spectroscopy data using statistical machine learning. *J. Open Source Softw.* **10**, 6256 (2025).
43. Jiang, X. et al. Interstitial-substitutional-mixed solid solution of RuO_2 nurturing a new pathway beyond the activity-stability linear constraint in acidic water oxidation. *Adv. Mater.* **37**, 2503354 (2025).
44. Patel, A. M., Nørskov, J. K., Persson, K. A. & Montoya, J. H. Efficient Pourbaix diagrams of many-element compounds. *Phys. Chem. Chem. Phys.* **21**, 25323–25327 (2019).
45. Chen, T. & Guestrin, C. XGBoost: a scalable tree boosting system. In *Proc. 22nd ACM SIGKDD International Conference on Knowledge Discovery and Data Mining* 785–794 https://doi.org/10.1145/2939672.2939785 (ACM, 2016).
46. Zhu, W. et al. Direct dioxygen radical coupling driven by octahedral ruthenium–oxygen–cobalt collaborative coordination for acidic oxygen evolution reaction. *J. Am. Chem. Soc.* **145**, 17995–18006 (2023).
47. Li, L. et al. Spin-polarization strategy for enhanced acidic oxygen evolution activity. *Adv. Mater.* **35**, 2302966 (2023).
48. Shen, Y. et al. Cr dopant mediates hydroxyl spillover on RuO_2 for high-efficiency proton exchange membrane electrolysis. *Nat. Commun.* **15**, 7861 (2024).

Acknowledgements

The authors acknowledge support from the Alliance for AI-Accelerated Materials Discovery (A3MD), which includes funding from Total Energies SE, Meta and BP. This research was undertaken thanks in part to funding provided to the University of Toronto's Acceleration Consortium from the Canada First Research Excellence Fund (grant number CFREF-2022-00042).

Author contributions

J.H.-S. and E.H.S. supervised the project. Y.B. and K.L. conceived the project idea and workflow. Y.B. performed materials synthesis, OER performance measurements and characterization investigations. K.L. built the ML workflow and models. N.H. performed OER performance measurements and characterization investigations. J.K. performed XRF measurements. R.Z. performed characterization investigations. S.M. performed XRD measurements. A.S.Z. performed X-ray photoelectron spectroscopy measurements. Y.L. performed OER measurements. S.H., J.E.H. and D.S. provided suggestions and feedback on the materials synthesis and mechanistic investigations. Y.B., K.L., A.S.Z., B.R.S., K.C., E.H.S. and J.H.-S. wrote and edited the paper. All the authors contributed to the discussion of the results and the final paper preparation.

Competing interests

The authors declare no competing interests.

Additional information

Supplementary information The online version contains supplementary material available at https://doi.org/10.1038/s41929-025-01463-x.

Correspondence and requests for materials should be addressed to Edward H. Sargent or Jason Hattrick-Simpers.

Peer review information *Nature Catalysis* thanks Milad Abolhasani, Olga Kasian and the other, anonymous, reviewer(s) for their contribution to the peer review of this work.